

Supplementary Materials for

Emergent ferromagnetism near three-quarters filling in twisted bilayer graphene

Aaron L. Sharpe*, Eli J. Fox*, Arthur W. Barnard, Joe Finney, Kenji Watanabe,
Takashi Taniguchi, M. A. Kastner, David Goldhaber-Gordon†

*These authors contributed equally to this work.

†Corresponding author. Email: goldhaber-gordon@stanford.edu

Published 25 July 2019 on *Science* First Release

DOI: 10.1126/science.aaw3780

This PDF file includes:

Materials and Methods
Supplementary Text
Figs. S1 to S10
References

Materials and Methods

Our device consists of twisted bilayer graphene (TBG) fully encapsulated in two hexagonal boron nitride (hBN) cladding layers, each \sim 50 nm thick. The heterostructure was assembled using a Poly(Bisphenol A carbonate) film/gel (Gel-Pak DGL-17-X8) stamp on a glass slide heated to 60 °C (4, 65). The stamp was first used to pick up the top hBN flake. Then, to stack two layers of graphene at a well defined twist angle, we used the van der Waals attraction between hBN and an exfoliated monolayer graphene flake to tear and pick up a portion of monolayer graphene from the larger flake. We then controllably rotated and picked up the remaining portion of the monolayer graphene (4, 16). This process allows us to stack two layers of monolayer graphene to within $\pm 0.2^\circ$, with the precision limited by motion of the flake during the tearing process. The completed stack was transferred onto 300-nm-thick SiO₂ atop a degenerately doped Si substrate which is used as a back gate.

A Ti/Au top gate was deposited onto the completed heterostructure, and was subsequently used as a hard mask for a CHF₃/O₂ (50/5 sccm) etch to define a Hall bar region. During the mesa etch, the heterostructure was protected by resist extending outward from the hard mask near each of the leads of the Hall bar to provide space for making Cr/Au edge contacts (66) without risk of shorting to the top gate. Throughout all processing, the sample temperature was kept below 180 °C to prevent potential relaxation of the twist angle of the TBG.

Using the Au top gate and the Si back gate, we can tune both the charge density in the TBG and the displacement field applied to the device. We model our gates as parallel plate capacitors such that the density under the top gated region is given by

$$n = C_{\text{BG}}(V_{\text{BG}} - V_{\text{BG}}^0) + C_{\text{TG}}(V_{\text{TG}} - V_{\text{TG}}^0),$$

where BG (TG) indicates the back (top) gate, C is the capacitance per unit area determined from low-density Hall slope measurements, and $(V_{\text{BG}}^0, V_{\text{TG}}^0)$ is the charge neutrality point (CNP) of the top gated region at zero displacement field. We define the applied displacement field as

$$D = (D_{\text{BG}} - D_{\text{TG}})/2,$$

where the displacement field within a given dielectric $D_i = \epsilon_i(V_i - V_i^0)/d_i$, ϵ_i is the relative dielectric constant, and d_i is the thickness of each dielectric. We assume a relative dielectric constant of $\epsilon_{\text{TG}} = 3$ for hBN. As we do not see any clear features to ascribe to a true zero in displacement field, we assume that when both gates are at 0 V, $D \approx 0$. This is a reasonable

assumption given that the expected displacement field due to the work function difference between the top and back gate is small (-0.01 V/nm). We expect any nonzero displacement field at zero gate voltages to simply yield a constant offset to our reported values of displacement field.

The device was measured in a dilution refrigerator reaching a base temperature of 30 mK. To obtain a low electron temperature in the device and to reduce high-frequency noise, the measurement lines are equipped with electronic filtering at the mixing chamber stage. Passing the wires through a cured mixture of epoxy and bronze powder filters GHz frequencies, while MHz frequencies are attenuated by low-pass RC filters mounted on sapphire plates for thermal anchoring. Four-terminal resistance measurements were performed with Stanford Research Systems SR830 lock-in amplifiers with NF Corporation LI-75A voltage preamplifiers, using a $1\text{ G}\Omega$ bias resistor to apply an AC bias current of 5 nA RMS at a frequency of 3.3373 Hz. Keithley 2400 SourceMeters were used to apply voltages to the gates. All standard Hall configuration measurements were performed using the same voltage probes. One voltage contact behaved inconsistently and was not used in any of the measurements.

Hysteresis loops with respect to DC current bias were performed in zero magnetic field, unless otherwise noted. The DC current was applied using a Yokogawa 7651 DC voltage source with a $100\text{ M}\Omega$ bias resistor. The differential resistance was then determined by measuring the response to an additional 5 nA AC current added to the DC current bias. The AC current was sourced from the lock-in amplifier using a $1\text{ G}\Omega$ bias resistor as before, and both the AC and DC current sources were connected to the source terminal on the sample using a tee. Since the resistance from the source terminal to ground through the device was much smaller than either of the two bias resistors, the currents were effectively added together.

Optical micrograph of the completed heterostructure

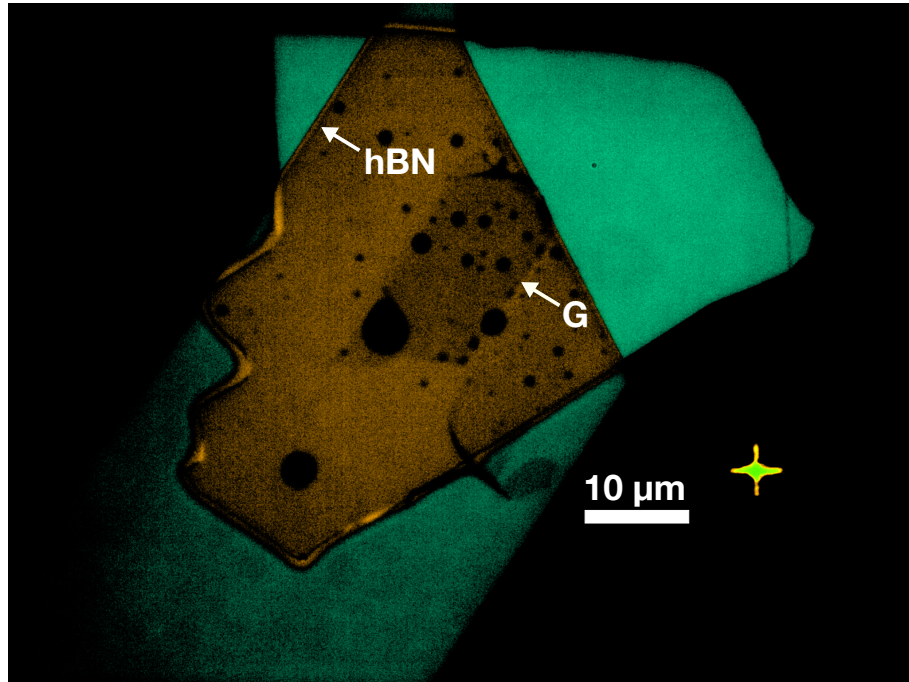


Figure S1: Micrograph of the TBG heterostructure. An optical micrograph of the completed heterostructure (before lithography) demonstrates the rotational alignment of the top hBN layer and graphene. The arrow labeled ‘G’ indicates a crystallographic edge of the top graphene layer of the TBG while the arrow labeled ‘BN’ indicates a crystallographic edge of the top encapsulating hBN crystal. Based on this micrograph, the alignment of the crystallographic edge of the top hBN to that of top graphene of the TBG is consistent with the experimentally measured angle of $\theta_{\text{hBN}} = 0.83^\circ \pm 0.02^\circ$ (calculated based on the density corresponding to the peak we associate with the hBN moiré pattern; see Fig. 1 of the main text). The bottom hBN is far from rotational alignment with the bottom graphene layer of the TBG.

Variability of the displacement field dependence between cooldowns

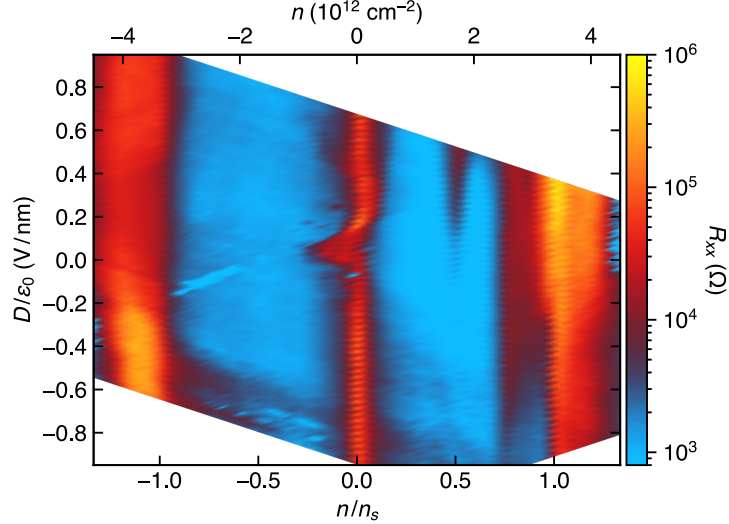


Figure S2: Displacement field dependence from separate cooldown. Longitudinal resistance R_{xx} of the TBG device (measured between contacts separated by 2.15 squares at 40 mK) as a function of carrier density n (shown on the top axis), filling factor relative to the superlattice density n_s (bottom axis), and the applied perpendicular displacement field D (left axis). This cooldown was separate from either of those described in the main text.

The dependence of the longitudinal resistance R_{xx} on displacement field is not perfectly reproducible between cooldowns. Fig. S2 shows a map of R_{xx} as a function n and D at $T = 40$ mK for a cooldown of the device separate from either of those described in the main text. When compared with Figure 1 of the main text, Fig. S2 appears to have an overall shift in D . In addition to this shift, there is an offset in the gate voltage corresponding to the resistance peak at the CNP that varies between cooldowns. We have accounted for this in calculating n and D . Comparing to Fig. 1 of the main text, this cooldown exhibits a broadening of the CNP resistance peak centered near 0.05 V/nm. Additionally, the position of the CNP resistance peak in the calculated density n does not appear to exhibit a significant change with D , aside from asymmetric broadening near $D = 0$ that disappears at larger $|D|$ (cf. Fig. 1 of the main text where the line traced by the peak in the 2D map appears to have a small kink). The differences between cooldowns are likely caused by variations in the disorder landscape seen by the TBG, which can be changed by thermal cycling the device. This variability between cooldowns did not impact our ability to observe magnetic hysteresis, which was present in each cooldown of the device in the dilution refrigerator.

Comparison with a second TBG device misaligned to hBN

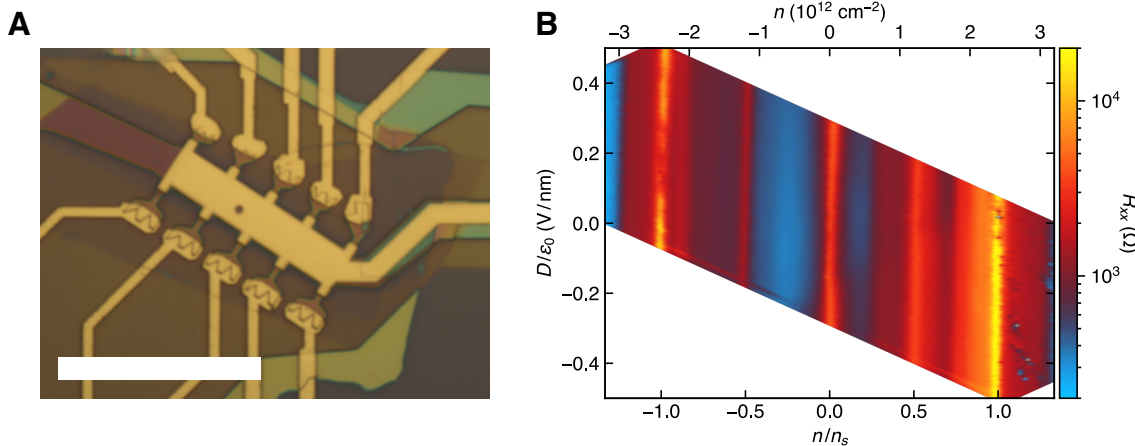


Figure S3: Displacement field dependence of TBG device misaligned to hBN. (A) An optical micrograph of the completed device. The scale bar is $20 \mu\text{m}$. (B) Longitudinal resistance R_{xx} of the misaligned TBG device (measured between contacts separated by 1.25 squares at 1.5 K) as a function of carrier density n (shown on the top axis, or as a filling factor relative to the superlattice density shown on the bottom axis) and perpendicular displacement field D .

To explain the dependence of transport on the direction of the displacement field in the device presented in the main text, we can compare it to the dependence in a second TBG device (with a $1.05^\circ \pm 0.02^\circ$ twist angle) where the graphene has been intentionally misaligned with each of the hBN cladding layers. This second device has an additional graphite back gate that should help to drastically reduce disorder of the potential landscape within the TBG by screening the effect of charges in the SiO_2 (19). Also replacing the top metal gate with a second graphite gate could lead to further improvement (6, 67).

When the longitudinal resistance is measured as a function of the applied gate voltages, this device shows drastically different dependence on the applied displacement field than the device of the main text. With the graphene misaligned with both hBN layers, the device is in an approximately symmetric dielectric environment (up to differences in disorder, hBN thicknesses, and gate materials). As a result, the longitudinal resistance has no features that strongly depend on the direction of the displacement field.

The stark contrast between the displacement field dependence of this misaligned device and the device of the main text suggests that the vertical symmetry of the heterostructure is broken in the latter. This could result from disorder, but as discussed in the main text, it appears that

the symmetry is broken by the alignment of one of the two hBN cladding layers with the TBG. The device with misaligned hBN also did not show AH effect at any filling.

Repeatability of hysteresis loops

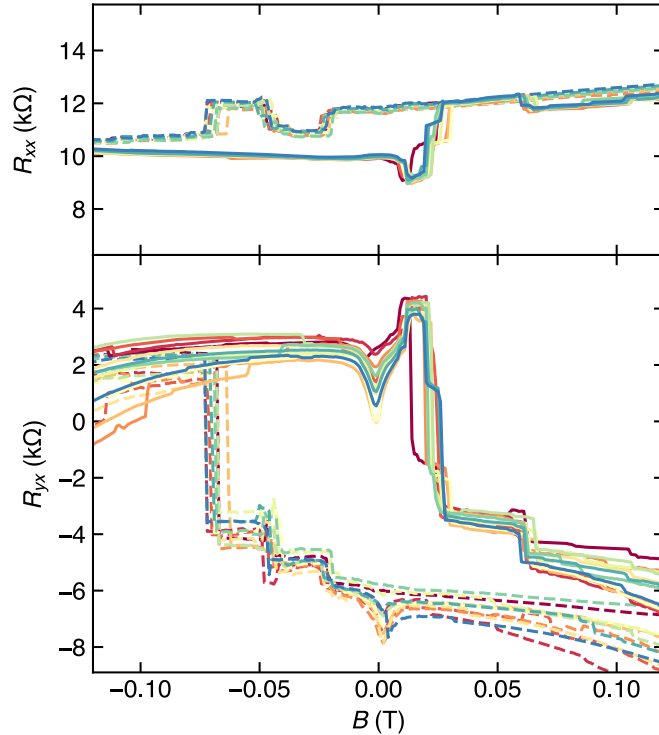


Figure S4: Repeated hysteresis loops. Longitudinal resistance R_{xx} (top panel) and Hall resistance R_{yx} (bottom panel) are shown as a function of magnetic field for twelve consecutive loops of the field between ± 250 mT for $n/n_s = 0.758$ and $D/\epsilon_0 = 0$ V/nm (in the same cooldown as that of Fig. S2). The solid and dashed lines correspond to measurements taken while sweeping the magnetic field B up and down, respectively.

To check the repeatability of the magnetic field dependence of transport, we swept the applied magnetic field between ± 250 mT twelve times while maintaining a constant density and displacement field (Fig. S4). The structure of the hysteresis loop is very consistent between sweeps with many of the intermediate jumps appearing highly repeatable. These jumps likely correspond to some magnetic domain structure with domains of varying coercivities, or to a repeatable pattern of domain wall motion and pinning. As discussed in the main text, this behavior may result from inhomogeneity caused by local variations in effective gating or in the

twist angle between the graphene sheets. Additionally, we see a dip (of unknown origin) in the Hall resistance on the advanced side of zero field for both directions of the hysteresis loop.

Extracting anomalous and conventional components of Hall effect

To clearly separate the two components of the Hall effect, we define the anomalous component as half the difference between $B = 0$ Hall signals on the up and down sweeps of applied field: $R_{yx}^{\text{AH}} = |R_{yx}^{\uparrow} - R_{yx}^{\downarrow}|/2$, where $R_{yx}^{\uparrow(\downarrow)}$ is the Hall resistance remaining at zero field after the sample has been magnetized by an upward (downward) applied field. If we took $R_{yx}^{\uparrow(\downarrow)}$ to equal the raw values of $R_{yx}(B = 0)$ under the two sweep directions, our reported parameters would be affected by small jumps in the resistance close to zero field. Instead, in analyzing the data, we examine a sweep toward zero field from a positive (negative) field higher than the coercive field; starting at a chosen high field cutoff, we include data until the first significant jump in R_{yx} . We fit a line to this subset and extrapolate or interpolate the value at $B = 0$ to estimate $R_{yx}^{\uparrow(\downarrow)}$. By varying the high field cutoff, we can estimate the uncertainty in the fitting parameters. We use the slope of these same linear fits as a measure of the conventional component of the Hall signal, R_H .

Extended discussion of nonlocal measurements

For completeness, we elaborate here on the discussion in the main text of our expectations for nonlocal measurements in different scenarios and how they compare to our results. Our primary conclusion from the data presented in the main text is that the nonlocal measurements do not correspond to either homogeneous conduction purely in the 2D bulk or the perfect chiral edge transport of an ideal quantum anomalous Hall (QAH) state (the case of a homogeneous Chern insulator). Instead, we argue that they are consistent with the existence of chiral edge states in combination with another dissipative transport mechanism or chiral transport along a network of domain walls. Below, we explain these scenarios in greater detail.

As introduced earlier, an ideal QAH state is characterized by an insulating 2D bulk and chiral edge states, which conduct without dissipation. Floating ohmic contacts equilibrate with the chiral edge states that propagate into them (31), and therefore take on the potential of either the source or the drain contact (in the absence of non-ideal contact resistances), depending on the chirality of the edge states. In a ferromagnetic QAH insulator, this chirality is determined by the direction of the magnetization, leading to hysteresis in the Hall resistance as a function of

applied magnetic field. The number of edge modes, each contributing e^2/h to the source-drain conductance, is given by the Chern number C , leading to a source-drain resistance of h/Ce^2 . As a result, when a current I flows from source to drain, floating terminals will have a voltage of either hI/Ce^2 or 0, referenced to the drain, if the contact is forward along the edge state direction of flow from the source or drain, respectively. Three-terminal resistances (such as $R_{54,14}$ in Fig. 3 of the main text), therefore, will be either h/Ce^2 or 0 and will alternate between the two if the chirality is reversed. With non-ideal contacts, three-terminal resistances will also be offset by an additional contact resistance from the drain. Four-terminal resistances, on the other hand, should always be 0 if measured between two voltage contacts on the same side of the perimeter relative to the source and drain, as is the case in the nonlocal configuration in which we measured (the four-terminal resistance $R_{54,12}$ in Fig. 3).

The case of transport via the 2D bulk in the absence of edge states is different in large part because of the nonzero longitudinal resistivity ρ_{xx} . The voltage of floating contacts will depend not only on the Hall resistivity ρ_{yx} , but will also pick up a contribution from ρ_{xx} times a geometrical factor (in addition to an offset from the drain contact resistance) that may be a significant fraction of the two-terminal source-drain resistance. For bulk transport with a relatively small Hall angle (the common case for an anomalous Hall effect, where typically $\rho_{yx}/\rho_{xx} \sim 0.1$ or less (38)), three-terminal resistances in a geometry like that of our nonlocal measurement configuration should differ between opposite magnetizations by a relatively small amount compared to their average value since the contribution from ρ_{xx} dominates, though this difference could be significant if the Hall angle is instead large. As in the QAH case, four-terminal resistances between contacts on the same side of the perimeter should not depend on the sign of the magnetization (32). Although nonzero, the four-terminal resistance in a nonlocal configuration similar to ours will be exponentially small: if current is passed between two contacts on one end of a long, thin strip while the voltage difference is measured between two contacts on the opposite end, the resulting nonlocal resistance from bulk conduction alone is $R_{NL}^{4T} \approx (\rho_{xx}/\pi) \exp(-\pi l/w)$, where l and w are the length and width of strip, respectively (32).

An additional possibility is that chiral edge states are present along with some other dissipative conduction channels. While carriers are only transmitted in one direction between adjacent pairs of contacts in an ideal QAH state, in this case backscattering between contacts in the opposite direction becomes possible through the additional channel, leading to nonzero four-terminal resistances. One such scenario, analyzed in Ref. 33, is a QAH state with additional, non-chiral edge states. Compared to the ideal QAH case, the presence of this channel allowing transmis-

sion of carriers in the opposite direction of the chiral edge states leads to a reduced difference in the three-terminal resistances between opposite chiralities. Four-terminal nonlocal resistances are also expected to be relatively large in comparison to those in either a pure QAH effect or the case of bulk conduction without edge states, and can differ between opposite magnetizations; this phenomenon results from the combination of nonlocal transport from the chiral edge states along with dissipation due to backscattering. Similar effects can occur from the combination of chiral edge states and any conduction mechanism allowing such backscattering, including others that could be present in the TBG system: nonzero bulk conductivity due to a small or spatially varying gap, or additional one-dimensional conduction paths through the bulk along a network of magnetic domain walls (34, 35) (due to the Chern number changing sign between domains of opposite magnetization).

As discussed in the main text, our measurements appear to be best explained by this latter situation, with both chiral edge channels and some other conduction mechanism like those described above. The three-terminal resistance $R_{54,14}$ shown in Fig. 3 of the main text exhibits significant hysteresis and differs by a large but non-quantized value between the two magnetizations for the density where the AH effect is strongest. This measurement rules out an ideal QAH effect but is still suggestive of nonlocal transport along edge channels. The behavior of the four-terminal resistance $R_{54,12}$ at this density, with a hysteresis loop saturating at approximately $42\ \Omega$ and $240\ \Omega$ for upward and downward magnetization, respectively, is likewise inconsistent with a homogeneous Chern insulator state. However, it also excludes the possibility of homogeneous bulk transport, which would yield $R_{54,12} \approx 3\ \Omega$. Both of these nonlocal measurements are instead consistent with chiral edge transport in combination with another conduction path giving rise to dissipation, which is also likely the explanation for the large but non-quantized AH effect we observed in transport in a typical Hall measurement configuration (Fig. 2 of the main text).

Extended discussion on the nature of the observed AH effect

In this section, we further develop our discussion of the source of the AH effect we have observed, and explore why it is not quantized. As mentioned in the main text, an AH effect can either be intrinsic, arising from Berry curvature of the filled bands, or extrinsic, resulting from scattering mechanisms.

One cause of an extrinsic AH effect, skew scattering, is associated with a linear relationship $\sigma_{xy} \propto \sigma_{xx}$ (where σ_{xy} and σ_{xx} are the Hall and longitudinal conductivities, respectively), which is clearly inconsistent with our data: for datasets parameterized by either n/n_s or temperature, shown in Fig. S5 A and C, this relationship is highly nonlinear. However, distinguishing between intrinsic Berry curvature and the other extrinsic mechanism, side jump scattering, is more challenging. Generally, the observed AH effect is compared with the theoretical expectation for the intrinsic contribution (23), but a clear theoretical consensus does not yet exist in the literature in this case.

Instead, we have argued in the main text that the size of ρ_{yx}^{AH} compared to that in other AH materials is evidence that its source is intrinsic. We reiterate and expand on this comparison here. As mentioned, the largest Hall angle measured in our device is $\rho_{xy}/\rho_{xx} = 1.4$, whereas previously reported (extrinsic or intrinsic) AH materials yield $\rho_{xy}/\rho_{xx} \lesssim 0.2$ (38), except for the magnetic topological insulators exhibiting near-vanishing ρ_{xx} in the QAH effect. Further, we found ρ_{yx}^{AH} as large as $0.4h/e^2$, greater than in early magnetic topological insulators (39–41). The corresponding longitudinal resistivity of $0.3h/e^2$ is also comparable to that of the first samples of those same materials to display near-quantization of ρ_{yx} in zero field ($\rho_{yx} \geq 0.98h/e^2$) (24, 25).

We have also argued in the main text that the origin is topological based on the appearance of the AH effect in an apparent insulating state. When the Fermi level is in a gap at zero temperature, the extrinsic mechanisms cannot contribute to σ_{xy} (23). In these conditions, the system is in a Chern insulating state if the occupied bands carry a net Chern number, or in a trivial insulating state with $\sigma_{xy} = 0$ otherwise. As we have discussed, the state at three-quarters filling is evidently not a single-domain, ideal Chern insulator given that ρ_{xx} does not vanish. However, we believe that our data could be consistent with the presence of a small, topologically nontrivial gap. One piece of evidence for this is that the ordinary Hall slope passes through zero and changes sign near the value of n at which ρ_{yx}^{AH} is maximized (see Fig. 2B of the main text). A corresponding dip is seen in σ_{xx} as a function of n/n_s , shown in Fig. S5D.

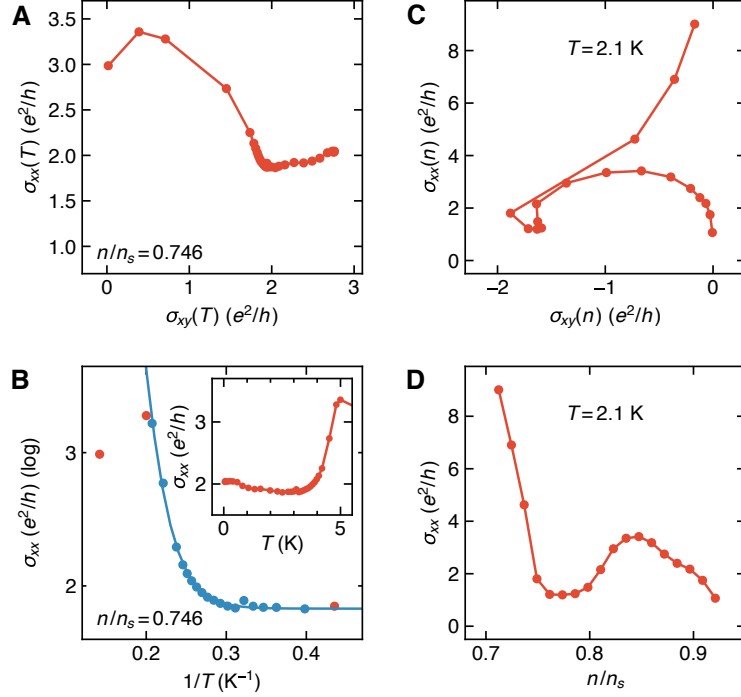


Figure S5: Behavior of the conductivity tensor. (A) The longitudinal conductivity σ_{xx} is plotted parametrically against the Hall conductivity σ_{xy} for a series of measurements at different temperatures with the density fixed at $n/n_s = 0.746$ and $D/\epsilon_0 = -0.62$ V/nm (shown in Fig. 2C of the main text). All conductivity values in this figure have been extracted from resistance measurements taken at 50 mT when sweeping the applied field downward from a value larger than the coercive field (so the sample has been magnetized by an upward field). The resistivity is derived from the measurements by assuming a homogeneous sample, and the conductivities are given by $\sigma_{xx} = \rho_{xx}/(\rho_{xx}^2 + \rho_{yx}^2)$ and $\sigma_{xy} = \rho_{yx}/(\rho_{xx}^2 + \rho_{yx}^2)$. The relationship between σ_{xy} and σ_{xx} is not consistent with an extrinsic AH effect resulting from skew scattering. (B) Arrhenius plot of σ_{xx} on a log scale versus $1/T$, with the same data shown in (A). The blue curve shows a fit of the data for $4.9 \text{ K} > T \geq 2.5 \text{ K}$ (the points shown in blue) to a model of activated conductivity with an additional, temperature-independent conduction channel (data points shown in red are excluded from the fit), yielding an estimated activation scale of $T_0 = 43$ K. (Inset) σ_{xx} is plotted on a linear scale against temperature. (C) σ_{xx} is plotted parametrically against σ_{xy} for a series of measurements at different densities at $T = 2.1$ K, with $D/\epsilon_0 = -0.22$ V/nm. These data were obtained during the same cooldown as that of the data shown in Figs. 1, 3, and 4 of the main text. Again, the behavior appears inconsistent with skew scattering. Moreover, it is qualitatively similar to the density dependence of the conductivity in a magnetic topological insulator approaching a QAH effect shown in Ref. 25. (D) σ_{xx} as a function of n/n_s , from the same data as in (C), showing the emergence of a dip in σ_{xx} around $n/n_s = 3/4$ consistent with the approach to a Chern insulator state.

In other studies of near-magic-angle TBG samples, a high-resistance state has also been observed at $n/n_s = 3/4$ (6, 7). They did not report large AH effect. The difference may be due to the alignment of the TBG with hBN in our experiment, as mentioned in the main text.

With nonlocal measurements also suggestive of edge state transport, we believe our collection of evidence suggests the system is approaching a Chern insulating state, but it remains to explain why it is non-ideal. There could be several reasons ρ_{yx} is not quantized and ρ_{xx} is nonzero, contrary to the expectation for a QAH effect. For one, the 2D bulk may not be strongly insulating, leading to both a nonzero ρ_{xx} and a reduction in the measured value of ρ_{yx} (39, 40).

Exploring the possibility of bulk conduction via the temperature dependence of σ_{xx} , we find that below 3 K some conduction mechanism persists, relatively insensitive to temperature (Fig. S5B). Between 3 K and 5 K, conductivity rises with increasing temperature, but this is not a large enough range to allow us to conclusively identify possible activated behavior in parallel with the temperature-insensitive conduction. Above 5 K, where the AH signal vanishes (see Fig. 2D of the main text), the conductance stops rising. We speculate that a substantial gap may only exist at lower temperatures in the magnetic phase. For the purpose of estimating a possible gap size, we can fit these data for $T < 4.9$ K to a model of activated conductivity with a parallel, temperature-independent conduction channel: $\sigma_{xx} = \sigma_0 e^{-T_0/T} + \sigma_1$, where T_0 is the thermal activation temperature scale, and σ_0 and σ_1 are constants. (In fact, σ_{xx} reaches a minimum and then increases slightly as the temperature decreases, as can be seen in the inset to Fig. S5B; we do not know the origin of this minimum, but we speculate that it could result from increasing mobility in a parallel channel at low temperature. To best estimate the possible gap size while avoiding complications from this behavior at the lowest temperatures, we also limit the fit range to exclude data at temperatures lower than 2.5 K, where σ_{xx} is minimized.) This fit yields an activation scale $T_0 = 43$ K, corresponding to an estimated gap of $\Delta = 2k_B T_0 = 7.5$ meV (including data at temperatures below 2.5 K makes the fit substantially worse but only modestly changes the fitted T_0 to 51 K). Although with a gap of this size, we might expect a well-quantized AH effect in our measurements at low temperature, the presence of an apparent additional conduction mechanism prevents this.

The low temperature residual conduction may be explained by inhomogeneity, which may result from local variations in twist angle or density, as we have noted elsewhere. Because of spatial variations in the density or gap size, it may be impossible to achieve a state in this sample with the Fermi level uniformly in the gap. Additionally, if such inhomogeneity results in a mixed domain state, edge states at domain walls could form a complex network resulting

in nonzero ρ_{xx} and non-quantized ρ_{yx} even at zero temperature, and even if the magnitude of the gap were uniform (see Refs. 34 and 35 for examples of very simple mixed domain configurations yielding significant ρ_{xx}). Given the signs of inhomogeneity we have observed, we suspect at least one of these scenarios may be realized in our sample. Even though such effects prevent the observation of a clear QAH effect, our results laid out in the main text and above nonetheless point to the existence of a topologically nontrivial gap opened by interactions.

The mechanism for opening such a topological gap remains to be determined. As we have discussed in the main text, interactions could spontaneously break the spin and valley symmetries, leaving 3 of the 4 flavors in the conduction miniband filled with the other empty (9). With a topological gap opened between the conduction and valence minibands, perhaps resulting from sublattice symmetry breaking due to the aligned hBN cladding layer, a Chern insulator state could thus exist at 3/4 filling. Alternatively, it could instead be the case that the 3/4 state is not both spin and valley polarized. For example, it is predicted that noncoplanar chiral magnetic order can give rise to a $C = 1$ Chern insulator state at 3/4 filling of a single (spinful) band in a Hubbard model on a triangular lattice (68). If the valley degeneracy is unbroken, a similar insulating state in TBG at 3/4 filling might have Chern number $C = 2$ from the contribution of each valley. Further study will be needed to clarify the exact nature of the apparent insulating state we have observed.

To be clear: the experimental data we present do not unambiguously demonstrate that the three-quarters state is a Chern insulator. A non-quantized AH effect could result from Berry curvature even if the Fermi level is not in a gap, though, as discussed above, the magnitude of the Hall angle observed here far exceeds that of any reported AH system not known to host a Chern insulator state.

Another possibility is an AH analogue to the Hall insulator (69, 70). In such a state, as $T \rightarrow 0$, $\rho_{xx} \rightarrow \infty$ while ρ_{xy} remains finite and nonzero, corresponding to $\sigma_{yx} \propto \sigma_{xx}^2 \rightarrow 0$. This alternative might be plausible given that the peak in R_{yx}^{AH} (Fig. 2 of the main text) occurs at a peak in R_{xx} (Fig. 1 of the main text) rather than at a minimum of R_{xx} as would be expected for a Chern insulating state. However, when we attempt to extract conductivities from our resistivity measurements, their temperature dependence appears inconsistent with a Hall insulator: with decreasing temperature, σ_{xx} initially falls but then saturates (Fig. S5B), and σ_{yx} increases (Fig. S5A). Furthermore, the Hall insulator state is not known to host topologically protected edge states, the presence of which is suggested by our nonlocal transport measurements.

Stability of the magnetization

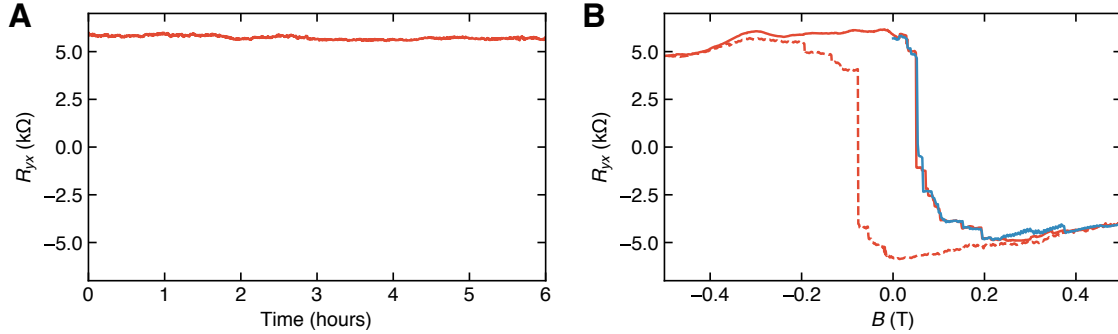


Figure S6: Temporal stability of the magnetization. **(A)** Hall resistance R_{yx} at $n/n_s = 0.746$ and $D/\epsilon_0 = -0.52$ V/nm as a function of time over the course of 6 hours in zero field, after first magnetizing the sample by applying -500 mT and then returning the field to 0 T. **(B)** A full hysteresis loop taken prior to the measurement shown in (A) is displayed in red. The blue trace shows the behavior of R_{yx} as the field is swept from 0 to 500 mT following the measurement in (A). A clear anomalous Hall jump in the blue trace is comparable to those in the continuous red loop, indicating that the magnetization was stable through the 6 hour pause.

Additional density dependence of hysteresis loops and effect of displacement field

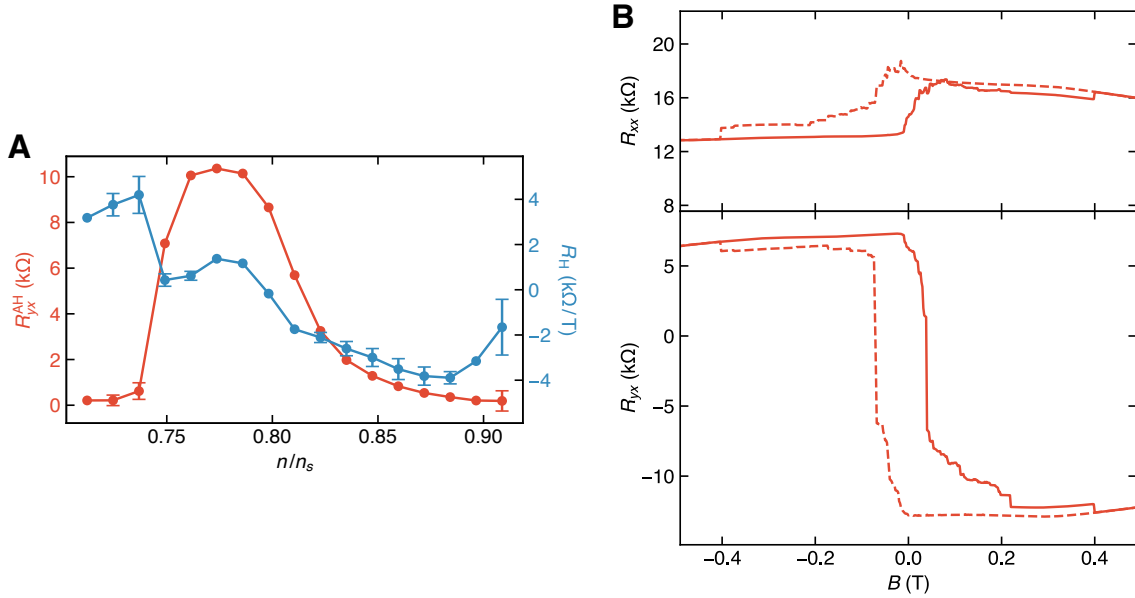


Figure S7: Density dependence near 3/4 with fixed displacement field at 2.1 K. (A) Zero-field anomalous Hall resistance R_{yx}^{AH} (red) and ordinary Hall slope R_H (blue) as a function of n/n_s while maintaining a constant displacement field $D/\epsilon_0 = -0.22$ V/nm. R_{yx}^{AH} is peaked at $n/n_s = 0.774$, close to the position of the peak at 0.758 in Fig. 2B of the main text and again coincident with a sign change in R_H . The full width at half maximum is slightly increased, at 0.07 instead of 0.04. **(B)** Magnetic field dependence of the longitudinal resistance R_{xx} (upper panel) and Hall resistance R_{yx} (lower panel) at $n/n_s = 0.774$, the largest hysteresis loop of the series shown in (A), with $R_{yx}^{AH} = 10.4$ kΩ.

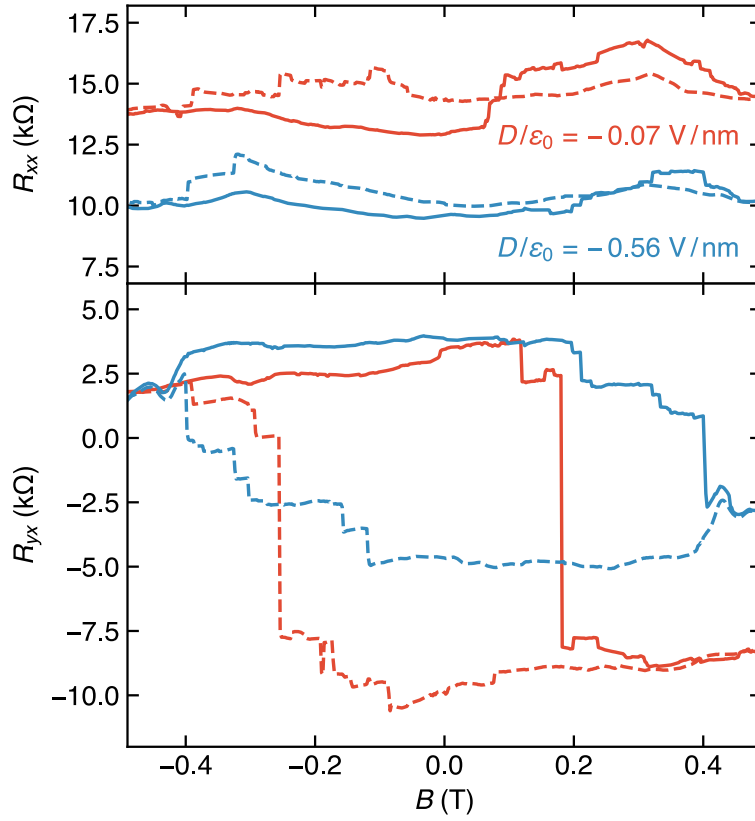


Figure S8: Displacement field dependence of hysteresis loops. Longitudinal resistance R_{xx} (upper panel) and Hall resistance R_{yx} (lower panel) at $n/n_s = 0.749$ for two different displacement fields as labeled in the figure. Although tuning the displacement field from a large negative field to near zero causes a slight change in the longitudinal resistance and the hysteresis loop structure, the TBG magnetic field dependence remains hysteretic.

Additional characterization of current-driven switching

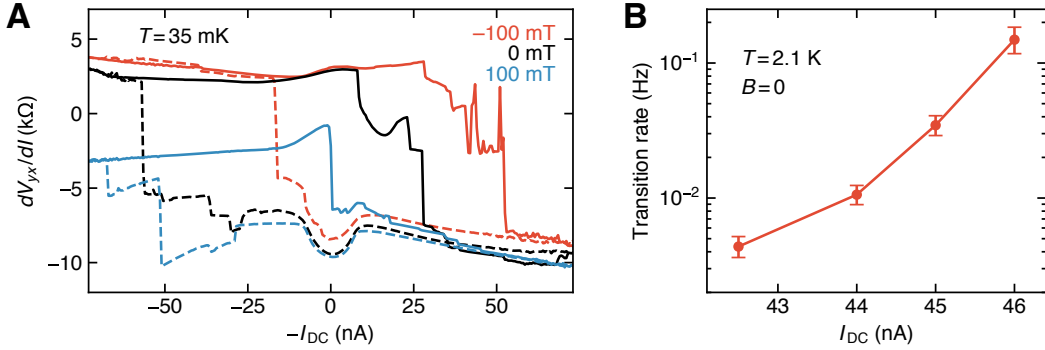


Figure S9: Current-driven switching in nonzero magnetic field, and characterization of the transition. (A) Hysteresis loops of the differential Hall resistance dV_{yx}/dI with respect to DC current (plotted as $-I_{DC}$ as in Fig. 4 of the main text) at three different static magnetic fields after the sample was magnetized at 500 mT. These data were taken at 35 mK with $n/n_s = 0.749$ and $D/\epsilon_0 = -0.22$ V/nm during the same cooldown as for the data of Fig. 4. (B) Transition rate of the apparent magnetization switching at a fixed current I_{DC} after magnetizing the sample with a -75 nA current (at $T = 2.1$ K and zero field). The transition appears to be a memoryless process.

The dependence of the DC current hysteresis loop (shown at zero field at $T = 2.1$ K in Fig. 4 of the main text) on applied field at $T = 35$ mK is shown in Fig. S9A. For each loop, the magnetic field was first increased to 500 mT and then decreased to the target field before cycling the DC current I_{DC} . Evidently, the applied field shifts the critical current required to switch the differential Hall resistance dV_{yx}/dI . Consistent with our expectation, when a nonzero field is applied, the magnitude of the current required to switch the apparent magnetization to the direction opposite (aligned) to the field is increased (decreased). It also appears from the loop at 100 mT that with sufficient field in the direction in which the sample has been magnetized, the DC current cannot completely reverse the magnetization, since dV_{yx}/dI remains significantly lower after switching than it does in the loops at 0 or -100 mT.

We further attempted to study the dynamics of the switching transition by measuring the time dependence of the differential Hall signal when I_{DC} was close to a value at which we observe large jumps in the loop shown in Fig. 4 of the main text. With the current fixed near the jump at ~ 45 nA, dV_{yx}/dI appears stable for a short time before rapidly switching (we did not measure the switching time itself since our lock-in measurements could not resolve changes

on a time scale faster than ~ 1 s). By repeatedly bringing I_{DC} to -75 nA and back to a target current near the jump (at a rate of 0.7 nA/s), then measuring dV_{yx}/dI as a function of time, we were able to investigate the statistics of this time lapse before the transition occurred. We find that the delay time before the switch appears to be exponentially distributed, indicating that the transition is a memoryless process that does not depend on the total charge transported. The corresponding transition rate (Fig. S9B) rapidly increases with I_{DC} near the currents at which we observe jumps in the full hysteresis loops, which were obtained by sweeping I_{DC} slowly at an average rate of 0.15 nA/s.

Quantum oscillations

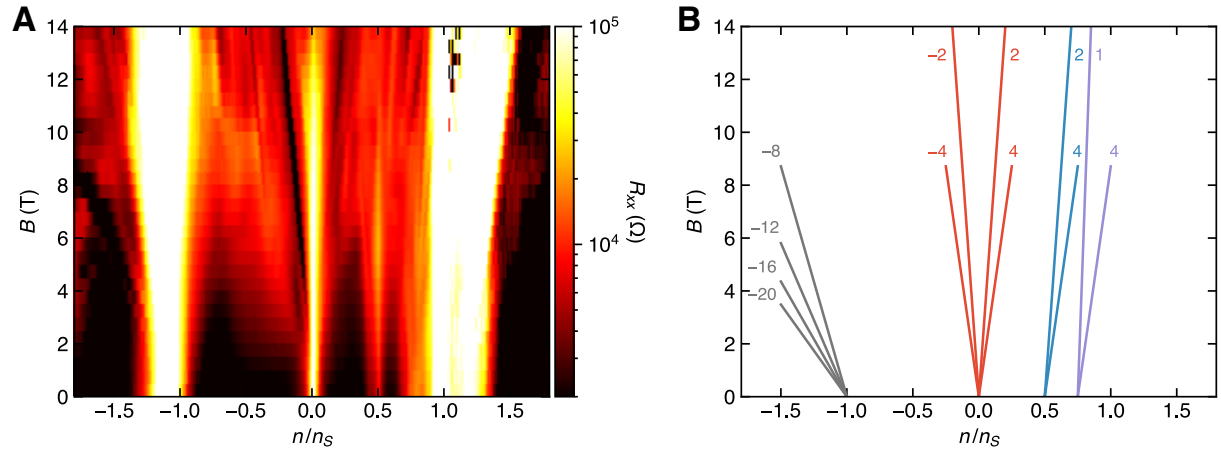


Figure S10: Quantum oscillations of TBG at fixed displacement field. (A) Landau fan diagram of the longitudinal resistance R_{xx} taken at 2.1 K for a fixed displacement field $D/\epsilon_0 = 0$ V/nm. Emerging from the CNP, we observe the Landau levels $\nu = \pm 2, \pm 4$. We further observe Landau levels from $n/n_s = 1/2$ of $\nu = 2, 4$, from $n/n_s = 3/4$ of $\nu = 1, 4$, and the sequence from $n/n_s = -1$ of $\nu = -8, -12, -16, -20$. (B) Schematic of the Landau levels observed in (A).

We observe several sets of Landau fans emerging from the high resistance states of the TBG (Fig. S10A). The discernible quantum oscillations are represented schematically in Fig. S10B. The degeneracy of Landau levels is representative of the symmetries of the electronic band structure and may yield information about where spin, valley, or layer symmetry may be broken.

Emerging from the CNP, the $\nu = \pm 2$ and ± 4 Landau levels are clearly visible. This is slightly surprising as one might expect the level sequence to reflect spin and valley degeneracies,

and hence four-fold degenerate Landau levels, as has been seen previously in magic angle TBG samples (6, 7). In the fan emerging from $n/n_s = 1/2$, we see similar periodicity with signs of $\nu = 2$ and 4. Additionally, there is a strong enhancement of the resistance at $n/n_s = 1/2$ with the applied out-of-plane magnetic field, peaking at roughly 6 T, in contrast to the behavior of the apparent correlated insulating state observed by Cao *et al.* (5). The $n/n_s = 3/4$ fan exhibits a further reduction of the periodicity such that we only observe clear signatures of $\nu = 1$ and 4. This reduction in symmetry at $n/n_s = 3/4$ could reflect interaction-driven lifting of the degeneracies: if the conduction bands for three spin-valley flavors are fully filled, we may be observing the quantum oscillations of a single flavor. No clear quantum oscillations emerge from $n/n_s = 1$, but the presence of $\nu = -8, -12, -16$, and -20 levels originating from $n/n_s = -1$ is consistent with what has been seen in other TBG samples (6, 7).

Absence of anomalous Hall effect at 1/4 filling

The state at $n/n_s = 1/4$ might be expected to behave similarly to the $3/4$ state due to the possible breaking of spin and valley degeneracies. Although we see signatures of a correlated state at $1/4$ filling (see the resistance peak at $1/4$ for positive displacement field in Fig. 1 of the main text), we were unable to observe an AH effect near the $1/4$ state. Theoretical calculations (9) indicate that interactions modify the band dispersion differently at different commensurate fillings. Empirically, it is clear that the prominence of the resistance peaks and the displacement field dependence differs significantly between $1/4$ and $3/4$, suggesting that the correlated states at the two fillings are not equivalent.

References and Notes

1. R. Bistritzer, A. H. MacDonald, Moire bands in twisted double-layer graphene. *Proc. Natl. Acad. Sci. U.S.A.* **108**, 12233–12237 (2011). [doi:10.1073/pnas.1108174108](https://doi.org/10.1073/pnas.1108174108) Medline
2. S. Fang, E. Kaxiras, Electronic structure theory of weakly interacting bilayers. *Phys. Rev. B* **93**, 235153 (2016). [doi:10.1103/PhysRevB.93.235153](https://doi.org/10.1103/PhysRevB.93.235153)
3. N. N. Nam, M. Koshino, Lattice relaxation and energy band modulation in twisted bilayer graphene. *Phys. Rev. B* **96**, 075311 (2017). [doi:10.1103/PhysRevB.96.075311](https://doi.org/10.1103/PhysRevB.96.075311)
4. Y. Cao, J. Y. Luo, V. Fatemi, S. Fang, J. D. Sanchez-Yamagishi, K. Watanabe, T. Taniguchi, E. Kaxiras, P. Jarillo-Herrero, Superlattice-induced insulating states and valley-protected orbits in twisted bilayer graphene. *Phys. Rev. Lett.* **117**, 116804 (2016). [doi:10.1103/PhysRevLett.117.116804](https://doi.org/10.1103/PhysRevLett.117.116804) Medline
5. Y. Cao, V. Fatemi, A. Demir, S. Fang, S. L. Tomarken, J. Y. Luo, J. D. Sanchez-Yamagishi, K. Watanabe, T. Taniguchi, E. Kaxiras, R. C. Ashoori, P. Jarillo-Herrero, Correlated insulator behaviour at half-filling in magic-angle graphene superlattices. *Nature* **556**, 80–84 (2018). [doi:10.1038/nature26154](https://doi.org/10.1038/nature26154) Medline
6. M. Yankowitz, S. Chen, H. Polshyn, Y. Zhang, K. Watanabe, T. Taniguchi, D. Graf, A. F. Young, C. R. Dean, Tuning superconductivity in twisted bilayer graphene. *Science* **363**, 1059–1064 (2019). [doi:10.1126/science.aav1910](https://doi.org/10.1126/science.aav1910) Medline
7. Y. Cao, V. Fatemi, S. Fang, K. Watanabe, T. Taniguchi, E. Kaxiras, P. Jarillo-Herrero, Unconventional superconductivity in magic-angle graphene superlattices. *Nature* **556**, 43–50 (2018). [doi:10.1038/nature26160](https://doi.org/10.1038/nature26160) Medline
8. J. Kang, O. Vafek, Strong coupling phases of partially filled twisted bilayer graphene narrow bands. *Phys. Rev. Lett.* **122**, 246401 (2019). [doi:10.1103/PhysRevLett.122.246401](https://doi.org/10.1103/PhysRevLett.122.246401)
9. M. Xie, A. H. MacDonald, On the nature of the correlated insulator states in twisted bilayer graphene. arXiv:1812.04213 [cond-mat.str-el] (11 December 2018).
10. M. Ochi, M. Koshino, K. Kuroki, Possible correlated insulating states in magic-angle twisted bilayer graphene under strongly competing interactions. *Phys. Rev. B* **98**, 081102 (2018). [doi:10.1103/PhysRevB.98.081102](https://doi.org/10.1103/PhysRevB.98.081102)
11. J. F. Dodaro, S. A. Kivelson, Y. Schattner, X. Q. Sun, C. Wang, Phases of a phenomenological model of twisted bilayer graphene. *Phys. Rev. B* **98**, 075154 (2018). [doi:10.1103/PhysRevB.98.075154](https://doi.org/10.1103/PhysRevB.98.075154)
12. A. Thomson, S. Chatterjee, S. Sachdev, M. S. Scheurer, Triangular antiferromagnetism on the honeycomb lattice of twisted bilayer graphene. *Phys. Rev. B* **98**, 075109 (2018). [doi:10.1103/PhysRevB.98.075109](https://doi.org/10.1103/PhysRevB.98.075109)
13. J. W. F. Venderbos, R. M. Fernandes, Correlations and electronic order in a two-orbital honeycomb lattice model for twisted bilayer graphene. *Phys. Rev. B* **98**, 245103 (2018). [doi:10.1103/PhysRevB.98.245103](https://doi.org/10.1103/PhysRevB.98.245103)
14. K. Seo, V. N. Kotov, B. Uchoa, Ferromagnetic Mott state in twisted graphene bilayers at the magic angle. *Phys. Rev. Lett.* **122**, 246402 (2019). [doi:10.1103/PhysRevLett.122.246402](https://doi.org/10.1103/PhysRevLett.122.246402)

15. B. Padhi, P. Phillips, Pressure-induced metal-insulator transition in twisted bilayer graphene. *Phys. Rev. B* **99**, 205141 (2019). [doi:10.1103/PhysRevB.99.205141](https://doi.org/10.1103/PhysRevB.99.205141)
16. K. Kim, M. Yankowitz, B. Fallahazad, S. Kang, H. C. P. Movva, S. Huang, S. Larentis, C. M. Corbet, T. Taniguchi, K. Watanabe, S. K. Banerjee, B. J. LeRoy, E. Tutuc, van der Waals heterostructures with high accuracy rotational alignment. *Nano Lett.* **16**, 1989–1995 (2016). [doi:10.1021/acs.nanolett.5b05263](https://doi.org/10.1021/acs.nanolett.5b05263) [Medline](#)
17. See supplementary materials.
18. J. B. Oostinga, H. B. Heersche, X. Liu, A. F. Morpurgo, L. M. K. Vandersypen, Gate-induced insulating state in bilayer graphene devices. *Nat. Mater.* **7**, 151–157 (2008). [doi:10.1038/nmat2082](https://doi.org/10.1038/nmat2082) [Medline](#)
19. B. Hunt, J. D. Sanchez-Yamagishi, A. F. Young, M. Yankowitz, B. J. LeRoy, K. Watanabe, T. Taniguchi, P. Moon, M. Koshino, P. Jarillo-Herrero, R. C. Ashoori, Massive Dirac fermions and Hofstadter butterfly in a van der Waals heterostructure. *Science* **340**, 1427–1430 (2013). [doi:10.1126/science.1237240](https://doi.org/10.1126/science.1237240) [Medline](#)
20. H. Yoo, R. Engelke, S. Carr, S. Fang, K. Zhang, P. Cazeaux, S. H. Sung, R. Hovden, A. W. Tsai, T. Taniguchi, K. Watanabe, G.-C. Yi, M. Kim, M. Luskin, E. B. Tadmor, E. Kaxiras, P. Kim, Atomic and electronic reconstruction at the van der Waals interface in twisted bilayer graphene. *Nat. Mater.* **18**, 448–453 (2019). [doi:10.1038/s41563-019-0346-z](https://doi.org/10.1038/s41563-019-0346-z) [Medline](#)
21. J. Xue, J. Sanchez-Yamagishi, D. Bulmash, P. Jacquod, A. Deshpande, K. Watanabe, T. Taniguchi, P. Jarillo-Herrero, B. J. LeRoy, Scanning tunnelling microscopy and spectroscopy of ultra-flat graphene on hexagonal boron nitride. *Nat. Mater.* **10**, 282–285 (2011). [doi:10.1038/nmat2968](https://doi.org/10.1038/nmat2968) [Medline](#)
22. S. Emori, C. K. Umachi, D. C. Bono, G. S. Beach, Generalized analysis of thermally activated domain-wall motion in Co/Pt multilayers. *J. Magn. Magn. Mater.* **378**, 98–106 (2015). [doi:10.1016/j.jmmm.2014.10.147](https://doi.org/10.1016/j.jmmm.2014.10.147)
23. N. Nagaosa, J. Sinova, S. Onoda, A. H. MacDonald, N. P. Ong, Anomalous Hall effect. *Rev. Mod. Phys.* **82**, 1539–1592 (2010). [doi:10.1103/RevModPhys.82.1539](https://doi.org/10.1103/RevModPhys.82.1539)
24. C.-Z. Chang, J. Zhang, X. Feng, J. Shen, Z. Zhang, M. Guo, K. Li, Y. Ou, P. Wei, L.-L. Wang, Z.-Q. Ji, Y. Feng, S. Ji, X. Chen, J. Jia, X. Dai, Z. Fang, S.-C. Zhang, K. He, Y. Wang, L. Lu, X.-C. Ma, Q.-K. Xue, Experimental observation of the quantum anomalous Hall effect in a magnetic topological insulator. *Science* **340**, 167–170 (2013). [doi:10.1126/science.1234414](https://doi.org/10.1126/science.1234414) [Medline](#)
25. J. G. Checkelsky, R. Yoshimi, A. Tsukazaki, K. S. Takahashi, Y. Kozuka, J. Falson, M. Kawasaki, Y. Tokura, Trajectory of the anomalous Hall effect towards the quantized state in a ferromagnetic topological insulator. *Nat. Phys.* **10**, 731–736 (2014). [doi:10.1038/nphys3053](https://doi.org/10.1038/nphys3053)
26. X. Kou, S.-T. Guo, Y. Fan, L. Pan, M. Lang, Y. Jiang, Q. Shao, T. Nie, K. Murata, J. Tang, Y. Wang, L. He, T.-K. Lee, W.-L. Lee, K. L. Wang, Scale-invariant quantum anomalous Hall effect in magnetic topological insulators beyond the two-dimensional limit. *Phys. Rev. Lett.* **113**, 137201 (2014). [doi:10.1103/PhysRevLett.113.137201](https://doi.org/10.1103/PhysRevLett.113.137201) [Medline](#)

27. E. J. Fox, I. T. Rosen, Y. Yang, G. R. Jones, R. E. Elmquist, X. Kou, L. Pan, K. L. Wang, D. Goldhaber-Gordon, Part-per-million quantization and current-induced breakdown of the quantum anomalous Hall effect. *Phys. Rev. B* **98**, 075145 (2018).
[doi:10.1103/PhysRevB.98.075145](https://doi.org/10.1103/PhysRevB.98.075145) Medline
28. R. Yu, W. Zhang, H.-J. Zhang, S.-C. Zhang, X. Dai, Z. Fang, Quantized anomalous Hall effect in magnetic topological insulators. *Science* **329**, 61–64 (2010).
[doi:10.1126/science.1187485](https://doi.org/10.1126/science.1187485) Medline
29. A. J. Bestwick, E. J. Fox, X. Kou, L. Pan, K. L. Wang, D. Goldhaber-Gordon, Precise quantization of the anomalous Hall effect near zero magnetic field. *Phys. Rev. Lett.* **114**, 187201 (2015). [doi:10.1103/PhysRevLett.114.187201](https://doi.org/10.1103/PhysRevLett.114.187201) Medline
30. C.-Z. Chang, W. Zhao, D. Y. Kim, P. Wei, J. K. Jain, C. Liu, M. H. W. Chan, J. S. Moodera, Zero-field dissipationless chiral edge transport and the nature of dissipation in the quantum anomalous Hall state. *Phys. Rev. Lett.* **115**, 057206 (2015).
[doi:10.1103/PhysRevLett.115.057206](https://doi.org/10.1103/PhysRevLett.115.057206) Medline
31. M. Büttiker, Absence of backscattering in the quantum Hall effect in multiprobe conductors. *Phys. Rev. B* **38**, 9375–9389 (1988). [doi:10.1103/PhysRevB.38.9375](https://doi.org/10.1103/PhysRevB.38.9375) Medline
32. L. J. van der Pauw, *Philips Res. Rep.* **13**, 1 (1958).
33. J. Wang, B. Lian, H. Zhang, S.-C. Zhang, Anomalous edge transport in the quantum anomalous Hall state. *Phys. Rev. Lett.* **111**, 086803 (2013).
[doi:10.1103/PhysRevLett.111.086803](https://doi.org/10.1103/PhysRevLett.111.086803) Medline
34. I. T. Rosen, E. J. Fox, X. Kou, L. Pan, K. L. Wang, D. Goldhaber-Gordon, Chiral transport along magnetic domain walls in the quantum anomalous Hall effect. *npj Quantum Mater.* **2**, 69 (2017). [doi:10.1038/s41535-017-0073-0](https://doi.org/10.1038/s41535-017-0073-0)
35. K. Yasuda, M. Mogi, R. Yoshimi, A. Tsukazaki, K. S. Takahashi, M. Kawasaki, F. Kagawa, Y. Tokura, Quantized chiral edge conduction on domain walls of a magnetic topological insulator. *Science* **358**, 1311–1314 (2017). [doi:10.1126/science.aan5991](https://doi.org/10.1126/science.aan5991) Medline
36. D. Apalkov, B. Dieny, J. M. Slaughter, Magnetoresistive random access memory. *Proc. IEEE* **104**, 1796–1830 (2016). [doi:10.1109/JPROC.2016.2590142](https://doi.org/10.1109/JPROC.2016.2590142)
37. P. Upadhyaya, Y. Tserkovnyak, Domain wall in a quantum anomalous Hall insulator as a magnetoelectric piston. *Phys. Rev. B* **94**, 020411 (2016).
[doi:10.1103/PhysRevB.94.020411](https://doi.org/10.1103/PhysRevB.94.020411)
38. E. Liu, Y. Sun, N. Kumar, L. Müchler, A. Sun, L. Jiao, S.-Y. Yang, D. Liu, A. Liang, Q. Xu, J. Kroder, V. Süß, H. Borrmann, C. Shekhar, Z. Wang, C. Xi, W. Wang, W. Schnelle, S. Wirth, Y. Chen, S. T. B. Goennenwein, C. Felser, Giant anomalous Hall effect in a ferromagnetic Kagomé-lattice semimetal. *Nat. Phys.* **14**, 1125–1131 (2018).
[doi:10.1038/s41567-018-0234-5](https://doi.org/10.1038/s41567-018-0234-5) Medline
39. J. G. Checkelsky, J. Ye, Y. Onose, Y. Iwasa, Y. Tokura, Dirac-fermion-mediated ferromagnetism in a topological insulator. *Nat. Phys.* **8**, 729–733 (2012).
[doi:10.1038/nphys2388](https://doi.org/10.1038/nphys2388)
40. C.-Z. Chang, J. Zhang, M. Liu, Z. Zhang, X. Feng, K. Li, L.-L. Wang, X. Chen, X. Dai, Z. Fang, X.-L. Qi, S.-C. Zhang, Y. Wang, K. He, X.-C. Ma, Q.-K. Xue, Thin films of

magnetically doped topological insulator with carrier-independent long-range ferromagnetic order. *Adv. Mater.* **25**, 1065–1070 (2013). [doi:10.1002/adma.201203493](#) [Medline](#)

41. X. Kou, M. Lang, Y. Fan, Y. Jiang, T. Nie, J. Zhang, W. Jiang, Y. Wang, Y. Yao, L. He, K. L. Wang, Interplay between different magnetisms in Cr-doped topological insulators. *ACS Nano* **7**, 9205–9212 (2013). [doi:10.1021/nn4038145](#) [Medline](#)
42. H. C. Po, L. Zou, A. Vishwanath, T. Senthil, Origin of Mott insulating behavior and superconductivity in twisted bilayer graphene. *Phys. Rev. X* **8**, 031089 (2018). [doi:10.1103/PhysRevX.8.031089](#)
43. L. Zou, H. C. Po, A. Vishwanath, T. Senthil, Band structure of twisted bilayer graphene: Emergent symmetries, commensurate approximants, and Wannier obstructions. *Phys. Rev. B* **98**, 085435 (2018). [doi:10.1103/PhysRevB.98.085435](#)
44. J. Kang, O. Vafek, Symmetry, maximally localized Wannier states, and a low-energy model for twisted bilayer graphene narrow bands. *Phys. Rev. X* **8**, 031088 (2018). [doi:10.1103/PhysRevX.8.031088](#)
45. M. Koshino, N. F. Q. Yuan, T. Koretsune, M. Ochi, K. Kuroki, L. Fu, Maximally localized Wannier orbitals and the extended Hubbard model for twisted bilayer graphene. *Phys. Rev. X* **8**, 031087 (2018). [doi:10.1103/PhysRevX.8.031087](#)
46. F. Amet, J. R. Williams, K. Watanabe, T. Taniguchi, D. Goldhaber-Gordon, Insulating behavior at the neutrality point in single-layer graphene. *Phys. Rev. Lett.* **110**, 216601 (2013). [doi:10.1103/PhysRevLett.110.216601](#) [Medline](#)
47. F. Amet, thesis, Stanford University (2014).
48. P. Moon, M. Koshino, Electronic properties of graphene/hexagonal-boron-nitride moiré superlattice. *Phys. Rev. B* **90**, 155406 (2014). [doi:10.1103/PhysRevB.90.155406](#)
49. M. Mucha-Kruczyński, J. R. Wallbank, V. I. Fal’Ko, Heterostructures of bilayer graphene and h-BN: Interplay between misalignment, interlayer asymmetry, and trigonal warping. *Phys. Rev. B* **88**, 205418 (2013). [doi:10.1103/PhysRevB.88.205418](#)
50. J. Jung, A. M. DaSilva, A. H. MacDonald, S. Adam, Origin of band gaps in graphene on hexagonal boron nitride. *Nat. Commun.* **6**, 6308 (2015). [doi:10.1038/ncomms7308](#) [Medline](#)
51. Y.-H. Zhang, D. Mao, Y. Cao, P. Jarillo-Herrero, T. Senthil, Nearly flat Chern bands in moiré superlattices. *Phys. Rev. B* **99**, 075127 (2019). [doi:10.1103/PhysRevB.99.075127](#)
52. N. Yeh, K. Sugihara, M. S. Dresselhaus, G. Dresselhaus, Transport properties and magnetic interactions in acceptor-type magnetic graphite intercalation compounds. *Phys. Rev. B* **40**, 622–635 (1989). [doi:10.1103/PhysRevB.40.622](#) [Medline](#)
53. P. Esquinazi, D. Spemann, R. Höhne, A. Setzer, K.-H. Han, T. Butz, Induced magnetic ordering by proton irradiation in graphite. *Phys. Rev. Lett.* **91**, 227201 (2003). [doi:10.1103/PhysRevLett.91.227201](#) [Medline](#)
54. A. W. Mombrú, H. Pardo, R. Faccio, O. F. de Lima, E. R. Leite, G. Zanelatto, A. J. C. Lanfredi, C. A. Cardoso, F. M. Araújo-Moreira, Multilevel ferromagnetic behavior of

- room-temperature bulk magnetic graphite. *Phys. Rev. B* **71**, 100404 (2005).
[doi:10.1103/PhysRevB.71.100404](https://doi.org/10.1103/PhysRevB.71.100404)
55. Y. Kopelevich, J. C. Medina Pantoja, R. R. da Silva, F. Mrowka, P. Esquinazi, Anomalous Hall effect in graphite. *Phys. Lett. A* **355**, 233–236 (2006).
[doi:10.1016/j.physleta.2006.02.034](https://doi.org/10.1016/j.physleta.2006.02.034)
56. J. Červenka, M. I. Katsnelson, C. F. J. Flipse, Room-temperature ferromagnetism in graphite driven by two-dimensional networks of point defects. *Nat. Phys.* **5**, 840–844 (2009).
[doi:10.1038/nphys1399](https://doi.org/10.1038/nphys1399)
57. P. Esquinazi, J. Krüger, J. Barzola-Quiquia, R. Schönemann, T. Herrmannsdörfer, N. García, On the low-field Hall coefficient of graphite. *AIP Adv.* **4**, 117121 (2014).
[doi:10.1063/1.4902099](https://doi.org/10.1063/1.4902099)
58. P. Zhou, C. Q. Sun, L. Z. Sun, Two dimensional antiferromagnetic Chern insulator: NiRuCl₆. *Nano Lett.* **16**, 6325–6330 (2016). [doi:10.1021/acs.nanolett.6b02701](https://doi.org/10.1021/acs.nanolett.6b02701) [Medline](#)
59. B. Lian, X.-Q. Sun, A. Vaezi, X.-L. Qi, S.-C. Zhang, Topological quantum computation based on chiral Majorana fermions. *Proc. Natl. Acad. Sci. U.S.A.* **115**, 10938–10942 (2018). [doi:10.1073/pnas.1810003115](https://doi.org/10.1073/pnas.1810003115) [Medline](#)
60. Q. L. He, L. Pan, A. L. Stern, E. C. Burks, X. Che, G. Yin, J. Wang, B. Lian, Q. Zhou, E. S. Choi, K. Murata, X. Kou, Z. Chen, T. Nie, Q. Shao, Y. Fan, S.-C. Zhang, K. Liu, J. Xia, K. L. Wang, Chiral Majorana fermion modes in a quantum anomalous Hall insulator-superconductor structure. *Science* **357**, 294–299 (2017). [doi:10.1126/science.aag2792](https://doi.org/10.1126/science.aag2792) [Medline](#)
61. A. C. Mahoney, J. I. Colless, L. Peeters, S. J. Pauka, E. J. Fox, X. Kou, L. Pan, K. L. Wang, D. Goldhaber-Gordon, D. J. Reilly, Zero-field edge plasmons in a magnetic topological insulator. *Nat. Commun.* **8**, 1836 (2017). [doi:10.1038/s41467-017-01984-5](https://doi.org/10.1038/s41467-017-01984-5) [Medline](#)
62. N. Bultinck, S. Chatterjee, M. P. Zaletel, Anomalous Hall ferromagnetism in twisted bilayer graphene. arXiv:1901.08110 [cond-mat.str-el] (23 January 2019).
63. Y.-H. Zhang, D. Mao, T. Senthil, Twisted Bilayer Graphene Aligned with Hexagonal Boron Nitride: Anomalous Hall Effect and a Lattice Model. arXiv:1901.08209 [cond-mat.str-el] (24 January 2019).
64. A. L. Sharpe, E. Fox, A. Barnard, J. Finney, K. Watanabe, T. Taniguchi, M. Kastner, D. Goldhaber-Gordon, Data for: Emergent ferromagnetism near three-quarters filling in twisted bilayer graphene, Version 1.0, Stanford Digital Repository (2019); <https://doi.org/10.25740/bg095cp1548>.
65. S. Bhandari, G.-H. Lee, A. Klales, K. Watanabe, T. Taniguchi, E. Heller, P. Kim, R. M. Westervelt, Imaging cyclotron orbits of electrons in graphene. *Nano Lett.* **16**, 1690–1694 (2016). [doi:10.1021/acs.nanolett.5b04609](https://doi.org/10.1021/acs.nanolett.5b04609) [Medline](#)
66. L. Wang, I. Meric, P. Y. Huang, Q. Gao, Y. Gao, H. Tran, T. Taniguchi, K. Watanabe, L. M. Campos, D. A. Muller, J. Guo, P. Kim, J. Hone, K. L. Shepard, C. R. Dean, One-dimensional electrical contact to a two-dimensional material. *Science* **342**, 614–617 (2013). [doi:10.1126/science.1244358](https://doi.org/10.1126/science.1244358) [Medline](#)

67. A. A. Zibrov, C. Kometter, H. Zhou, E. M. Spanton, T. Taniguchi, K. Watanabe, M. P. Zaletel, A. F. Young, Tunable interacting composite fermion phases in a half-filled bilayer-graphene Landau level. *Nature* **549**, 360–364 (2017). [doi:10.1038/nature23893](https://doi.org/10.1038/nature23893) [Medline](#)
68. I. Martin, C. D. Batista, Itinerant electron-driven chiral magnetic ordering and spontaneous quantum Hall effect in triangular lattice models. *Phys. Rev. Lett.* **101**, 156402 (2008). [doi:10.1103/PhysRevLett.101.156402](https://doi.org/10.1103/PhysRevLett.101.156402) [Medline](#)
69. S. Kivelson, D.-H. Lee, S.-C. Zhang, Global phase diagram in the quantum Hall effect. *Phys. Rev. B* **46**, 2223–2238 (1992). [doi:10.1103/PhysRevB.46.2223](https://doi.org/10.1103/PhysRevB.46.2223) [Medline](#)
70. M. Hilke, D. Shahar, S. H. Song, D. C. Tsui, Y. H. Xie, D. Monroe, Experimental evidence for a two-dimensional quantized Hall insulator. *Nature* **395**, 675–677 (1998). [doi:10.1038/27160](https://doi.org/10.1038/27160)